Hot carrier-mediated avalanche multiphoton photoluminescence from coupled Au–Al nanoantennas

Jiyong Wang, (iD) Anne-Laure Baudrion, Jérémie Béal, Anke Horneber, Feng Tang, Jérémy Butet, (iD) Olivier J. F. Martin, (iD) Alfred J. Meixner, Pierre-Michel Adam, and (iD) Dai Zhang

COLLECTIONS

Paper published as part of the special topic on Spectroscopy and Microscopy of Plasmonic Systems

View Online   Export Citation   CrossMark

ARTICLES YOU MAY BE INTERESTED IN

Hot carrier-mediated avalanche multiphoton photoluminescence from coupled Au–Al nanoantennas

View Online Export Citation CrossMark

Jiyong Wang,[1,2,3,4,a)] Anne-Laure Baudrion,[2] Jérémie Béal,[2] Anke Horneber,[1,3] Feng Tang,[2] Jérémy Butet,[5] Olivier J. F. Martin,[5] Alfred J. Meixner,[1,3] Pierre-Michel Adam ,[2,a)] and Dai Zhang[1,3,a)]

AFFILIATIONS

[1] Institute of Physical and Theoretical Chemistry, Eberhard Karls University of Tübingen, Auf der Morgenstelle 15, 72076 Tübingen, Germany

[2] Light, Nanomaterials and Nanotechnology, University of Technology of Troyes, 12 Rue Marie Curie, CS42060, 10004 Troyes Cedex, France

[3] Center for Light-Matter-Interaction, Sensors and Analytics (LISA+), Eberhard Karls University of Tübingen, Auf der Morgenstelle 15, 72076 Tübingen, Germany

[4] Key Laboratory of 3D Micro/Nano Fabrication and Characterization of Zhejiang Province, School of Engineering, Westlake University, 18 Shilongshan Road, 310024 Hangzhou, Zhejiang Province, China

[5] Nanophotonics and Metrology Laboratory (NAM), Swiss Federal Institute of Technology, Lausanne (EPFL), 1015 Lausanne, Switzerland

Note: This paper is a part of the JCP Special Topic on Spectroscopy and Microscopy of Plasmonic Systems.
[a)]**Authors to whom correspondence should be addressed:** wangjiyong@westlake.edu.cn; pierre_michel.adam@utt.fr; and dai.zhang@uni-tuebingen.de

ABSTRACT

Avalanche multiphoton photoluminescence (AMPL) is observed from coupled Au–Al nanoantennas under intense laser pumping, which shows more than one order of magnitude emission intensity enhancement and distinct spectral features compared with ordinary metallic photoluminescence. The experiments are conducted by altering the incident laser intensity and polarization using a home-built scanning confocal optical microscope. The results show that AMPL originates from the recombination of avalanche hot carriers that are seeded by multiphoton ionization. Notably, at the excitation stage, multiphoton ionization is shown to be assisted by the local electromagnetic field enhancement produced by coupled plasmonic modes. At the emission step, the giant AMPL intensity can be evaluated as a function of the local field environment and the thermal factor for hot carriers, in accordance with a linear relationship between the power law exponent coefficient and the emitted photon energy. The dramatic change in the spectral profile is explained by spectral linewidth broadening mechanisms. This study offers nanospectroscopic evidence of both the potential optical damages for plasmonic nanostructures and the underlying physical nature of light–matter interactions under a strong laser field; it illustrates the significance of the emerging topics of plasmonic-enhanced spectroscopy and laser-induced breakdown spectroscopy.

I. INTRODUCTION

Exhibiting fascinating linear and non-linear optical properties, plasmonic nanoantennas have been subjects of numerous investigations in recent years.[1–4] Their potential applications in a variety of fields, such as biosensing,[5,6] light harvesting systems,[7] and field effect transistors,[8,9] have motivated researchers to understand their fundamental physical properties and the optical processes they can support. Localized surface plasmon resonances (LSPRs) have attracted particular attention as they allow concentrating and enhancing the electromagnetic field in sub-wavelength volumes.[10–12] The influences of LSPRs on the linear optical properties of plasmonic

nanoantennas, such as the scattering, absorption, and single-photon photoluminescence (PL) emission, as well as the nonlinear optical properties, such as harmonic generations (HG) and multiphoton photoluminescence (MPL), have been investigated.[4,13–19]

Metallic PL was first observed by Morradian in 1969 from noble metal films, and the PL emission was classically attributed to the radiative recombination of electrons near the Fermi energy level with holes in the *d*-band.[20–23] Yet, with the development of nanotechnology, pieces of evidence also emerged that in some cases the PL spectra and energy from plasmonic nanostructure closely follow their far-field scattering or extinction spectral profiles.[24–27] These observations clearly demonstrated the involvement of LSPRs in the metallic PL; the PL emission is associated with the radiative decay from the LSPRs energy levels.[24–27] Thanks to those new observations, the PL, and especially MPL, of plasmonic nanoparticles (NPs) becomes crucial to understand the fundamental mechanisms of optical transitions in metallic nanoparticle and to explore their practical applications such as local emitters based on nonlinear processes, two-photon PL (TPL) imaging, and plasmonic saturable absorber.[28–31]

Ultrafast laser pulses are normally required to produce considerable MPL. The number of the absorbed photon for an optical transition, namely, the power law exponent coefficient, can be evaluated by the fitting slope in a double logarithmic coordinate, which plots the MPL intensity as a function of the incident laser intensity. Generally, the slope is not larger than two due to the fast relaxation of the first excited electron in the conduction band.[32] Nevertheless, a slope of up to 18 has been reported, for example, in the avalanche-like MPL from coupled Au nanowires.[33,34] Similar phenomena were observed from Ag nanowire arrays and monomers.[33,35,36] These high power laws were attributed to the local field enhancement induced by the surface plasmon resonance and to surface plasmon–assisted thermal radiation.[33,34] However, the complex underlying physical nature still needs to be clarified.

We report here the observation of giant avalanche multiphoton photoluminescence (AMPL) from coupled Au–Al nanodimers, which benefits from both the strong local field enhancement in the nanogap of the two constituting NPs and from their tunable coupled plasmonic modes.[19] The changes in the dependence of the power law exponent coefficient on the incident laser intensity, as well as the polarization and emission spectral shapes before and after the occurrence of AMPL, are systematically investigated. The underlying physical mechanisms are discussed considering Keldysh rate equations in a strong electromagnetic field regime. Here, "strong" is a relative term—opposite of "weak" or "perturbative"—which denotes that the laser intensity is beyond the optical breakdown threshold. Laser-induced breakdown spectroscopy and its microscopic hot carrier dynamics are investigated.

II. RESULTS

Au–Al heterodimers of different particle sizes and gap (edge-to-edge) distances have been measured. For simplification, the expression "AuD1-AlD2-gD3" represents a heterodimer that is composed of an Au NP with a diameter "D1" nm and an Al NP with a diameter of "D2" nm, which are "D3" nm (edge-to-edge gap) apart from each other. For the contacted heterodimers, the denotation for the gap distance is omitted. The AMPL is first observed from contacted Au–Al heterodimers and those with the smallest gaps. As compared to the PL before the AMPL occurrence, the AMPL intensity is more than one order of magnitude larger and shows a dramatic spectral change. The changes in spectral intensity and shape are irreversible when the incident laser intensity returns to its original value. The above observations are demonstrated in Figs. 1(a)–1(c), which shows optical measurements performed for a single contacted Au120–Al140 heterodimer excited using the same incident laser intensity. The incident beam is linearly polarized along the dimer long axis, as shown in Figs. 1(a) and 1(b). As can be seen
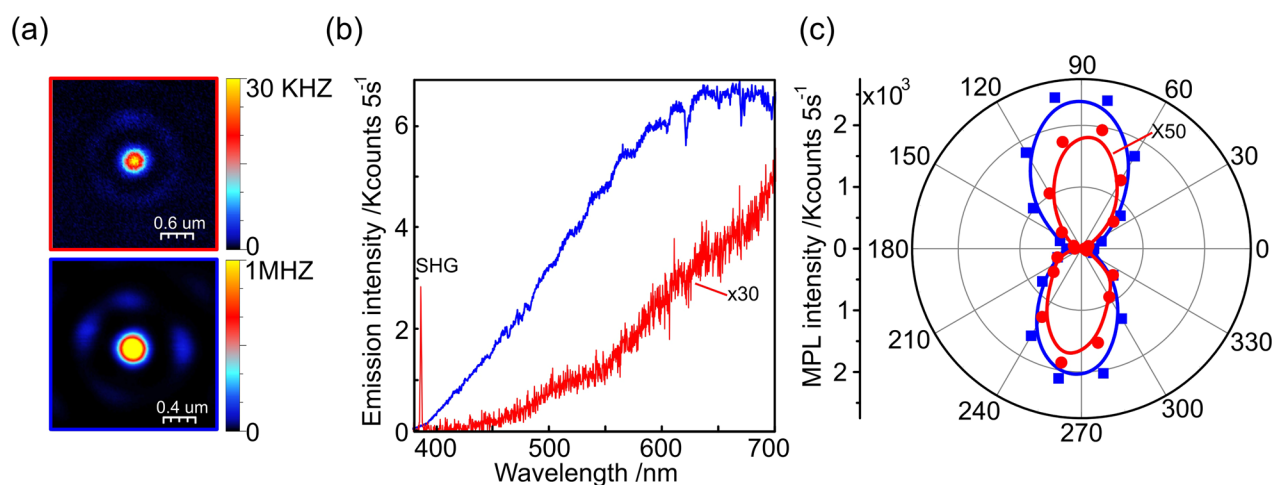
FIG. 1. (a) Confocal optical images before (upper picture) and after (lower picture) the occurrence of AMPL. The optical signals are collected from 350 nm to 680 nm. (b) The emission spectra before (red) and after (blue) the occurrence of AMPL. For better visibility, the red spectrum is multiplied by a factor of 30. (c) The dependence of spectrally integrated emission intensities (390 nm–700 nm) on the excitation polarization. The red dots represent the dependency before the occurrence of AMPL, which is multiplied by 50 for better visibility. The blue squares are those after the occurrence of AMPL. Figures 1(a)–1(c) are taken from the same single heterodimer Au120–Al140, and the incident beam is linearly polarized.
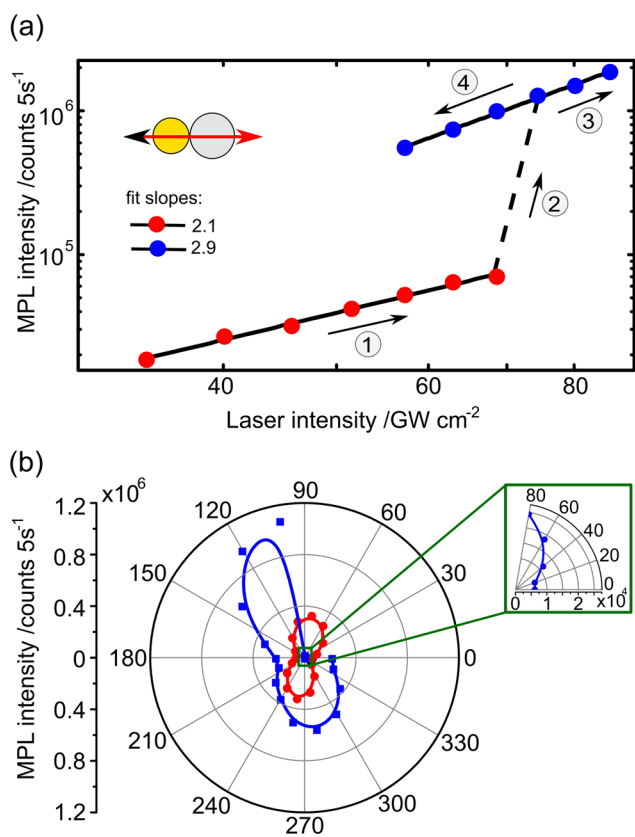
FIG. 2. (a) Double logarithmic plot of the MPL intensity from a single Au120–Al160 heterodimer as a function of the incident laser intensity. The incident beam is linearly polarized along the long dimer axis. We can distinguish four regimes with different excitation intensity dependences: ① pre-AMPL step, which is indicated by the red dots; ② AMPL occurring step, which is represented by the black dashed line; ③ post-AMPL step with continuous increase in the incident intensity until to the limit of the laser, which is indicated by the blue dots; ④ post-AMPL step with decreasing laser intensity until below the previous threshold, which is represented as blue dots. The fit slope from MPL at step 1 is 2.1, which increases to 2.9 at steps ③ and ④. (b) Excitation polarization–dependent MPL intensity measured from a single Au120–Al180 heterodimer. The dimer long axis is at around 80° at a weak excitation intensity. The integrated intensities are multiplied by a factor of 10 for better legibility. The blue dots and squares represent the experimental results obtained around the transition from step ① to ② at a stronger excitation intensity. The AMPL takes place during the step at which the excitation polarization angle changes from 80° to 100°.

from Fig. 1(a), the maximum intensity at the center of the Airy disk recorded with the AMPL occurrence (lower picture) is more than 30 times stronger than the one without (upper picture). The corresponding spectra are shown in Fig. 1(b), where the AMPL spectrum (shown in blue) is at least 30 times higher than the one mentioned earlier (shown in red). Notably, the SHG intensity decreases dramatically after the occurrence of AMPL. The dependence of spectrally integrated emission intensities (from 390 nm to 700 nm) on excitation polarization is shown in Fig. 1(c). The red dots represent the dependency before AMPL, which is multiplied by a factor of 50 for

better visibility. The blue squares are those after AMPL. The dipole-emission-like curves (red and blue) serve for guiding the eye. It can be seen that the dominant change comparing these two patterns is the intensity.

To identify the involvement of multi-photon processes and the presence of a threshold laser intensity that is able to trigger the AMPL signals, we have performed optical measurements on Au–Al heterodimers of varying geometries. A double logarithmic plot of the MPL intensity taken from a single contacted Au120–Al160 heterodimer as a function of the incident laser intensity is shown in Fig. 2(a). The incident beam is linearly polarized along the long dimer axis, as shown in the inset. We can distinguish four regimes with different excitation intensity dependences: ① pre-AMPL step, which is indicated by the red dots; ② AMPL step, which is represented by the dashed black line; ③ post-AMPL step with continuous increase in the incident intensity up to the applicable power-limit of the laser, which is indicated by the blue dots; ④ post-AMPL step with decreasing laser intensity until below the previous threshold, which is represented as blue dots as well. For the studied single contacted Au120–Al160 heterodimer, a laser intensity threshold of around 69 GW cm^{-2} is required to transit from step ① to ②. The fit slope at step ① is 2.1, which increases to 2.9 at steps ③ and ④, indicating that the number of photons involved per transition event changes from ② to ③.

Another strategy to trigger the AMPL without changing the incident power is to rotate the excitation polarization. As shown in Fig. 2(b), AMPL is triggered at a single contacted Au120–Al180 heterodimer via varying the excitation polarization from along the dimer short axis to the long axis. The dimer long axis is around 80°, as can be seen from the dipole-like emission pattern (red dots) at weak excitation intensity. The integrated PL intensities are multiplied by a factor of 10 for better legibility. The blue dots and squares represent the experimental results obtained around the transition from the pre-AMPL step to the post-AMPL step, which are excited with a stronger incident intensity (63 GW cm^{-2}). As highlighted in the inset of Fig. 2(b), the Au120–Al180 heterodimer exhibits a slightly increasing PL by turning the linear polarization from along the short dimer axis (0°) to nearly along the long dimer axis (approaching to 80°). Afterward, the AMPL takes place during the step at which the excitation polarization angle changes from 80° to 100°. The excitation polarization rotation step is 20°. The delay between two consecutive measurements is ~20 s.

III. DISCUSSIONS

The excitation of TPL from noble metals in the weak electromagnetic field regime is usually described via a sequential absorption of two single photons.[20,37,38] In this case, the electron in the conduction sp-band below the Fermi energy level E_f absorbing the first photon is excited above the E_f via intraband transition, which leaves a hole behind. The second photon excites an electron in the valence d-band, which recombines with the hole created in the previous excitation step. A hole in the d-band is then left. The recombination of the excited sp-band electron and d-band hole gives rise to the TPL. As shown in Fig. 3(a), the emission spectra for an Au monomer (blue), Al monomer (yellow), Al–Al dimer (black), Au–Au dimer (green), and Au–Al dimer (red) of the same diameter (160 nm) in
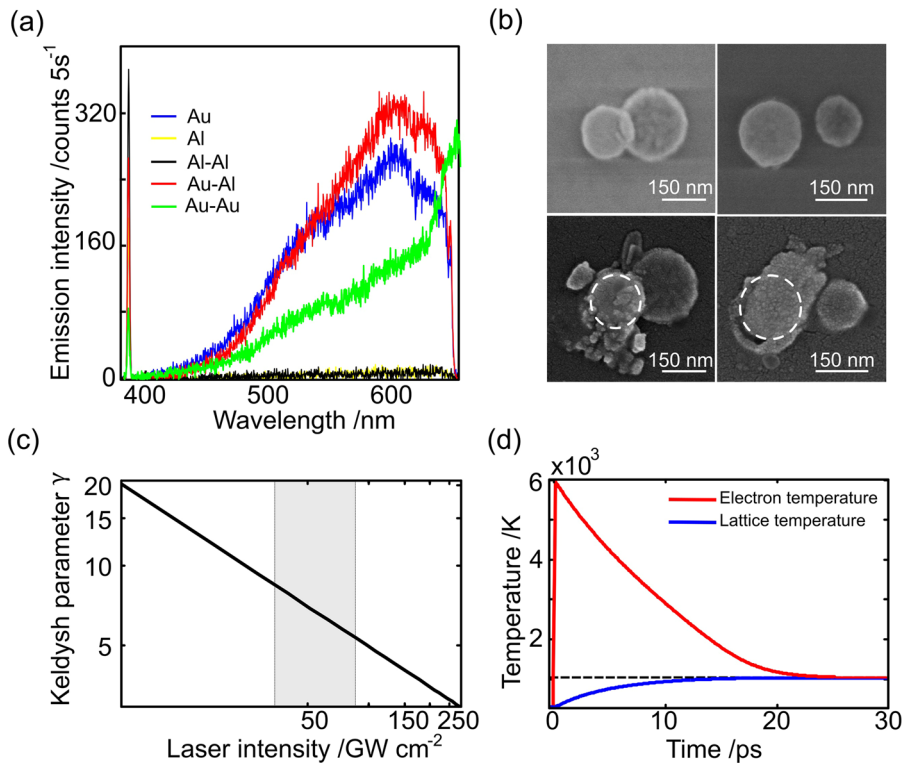
FIG. 3. (a) Emission spectra for an Au monomer (blue), Al monomer (yellow), Al–Al dimer (black), Au–Au dimer (green), and Au–Al dimer (red) in the weak electromagnetic field. The NPs have the same diameter (160 nm) and the dimers have no gap. The incident beam is linearly polarized along the dimer long axis. (b) The SEM images of contacted Au160–Al240 (left column) and Au 180–Al120–g40 (right column) heterodimers without (upper row) and with (lower row) the occurrence of AMPL. The white dashed rings indicate the original positions of Au NPs before AMPL occurs. (c) The calculated Keldysh parameter as a function of the incident laser intensity. (d) Calculated electron (red) and lattice (blue) temperature vs time according to the two-temperature model at the critical laser intensity of 70.6 GW cm^{-2}. The black horizontal dashed line represents the melting point of Au NPs: 1045 K.

the weak electromagnetic field are compared. It is clearly visible that for Al neither the monomer nor dimer gives strong TPL as it is for the Au NP. The potential reason could be the weaker near-field enhancement at the Al NP and its reduced crystallinity due to the native oxide layer.[39,40] Thus, the TPL signal from the heterodimers originates dominantly from the Au NP.

Before reaching the emission state, the excited electrons reach a thermal equilibrium through electron–electron and electron–phonon scattering.[41–43] The effect of fast (sub-ps) electron thermalization in the weak field regime is often omitted. However, in a strong electromagnetic field, quasi-free electrons in the conduction band can be generated through nonlinear processes such as multiphoton ionization or tunneling ionization.[44] More free carriers can be produced through cascade ionization once free charges gain sufficient kinetic energy from the electromagnetic field.[44] The rapid ionization leads to plasma formation and to a dramatic increase in the absorption coefficient, which in turn gives rise to a faster energy transfer from the electric field to the medium.[3,44,45] Collisional heating of the electrons occurs before they transfer the energy to the lattice. This heating and energy diffusion, seeded by multiphoton ionization and combined with cascade ionization, result in an electron avalanche.[46] The resulting large amount of hot electrons in the conduction bands and hot holes in the valence bands recombine and produce a high number of photons, corresponding to AMPL. Once the electron avalanche is triggered, either by increasing the incident beam intensity or enhancing the local electromagnetic field, further ionization will not stop until all the valence electrons are ionized.[45] When phonons gain high enough kinetic energy from hot electrons

such that their displacement corresponds to a fraction of the lattice constant, the material undertakes a phase transition to melt.[45] At sufficient high laser intensity, the lattice can be removed from the target surface through Coulomb explosion or thermal vaporization mechanisms.[47] Due to the space-charge effect and band structure modification,[47] e.g., higher crystallinity,[48] even at weak radiation field, the NPs still show a stronger power law dependence on laser intensity than those absent from AMPL,[47,49–51] as shown in Fig. 2(a). The SEM images of thermally damaged nanostructures are shown in Fig. 3(b). The Au NPs (left side of the dimer) are severely damaged (lower panel) after the occurrence of AMPL, compared with the case without optical measurements (upper panel). On the contrary, the Al NPs (right side of the dimer) approximately maintain their geometries even after the occurrence of AMPL. Based on Figs. 3(a) and 3(b), it is reasonable to attribute the generation of AMPL to the optical breakdown process of Au NPs induced by a strong electromagnetic field.

The ionization of the condensed medium induced by a strong electromagnetic field or a photoionization process has been quantitatively described by the Keldysh rate equations.[52] Photoionization consists of contributions from tunneling ionization and multiphoton ionization and the ratio between these two can be quantified via the Keldysh parameter γ.[46,52] When γ is larger than 1, the photoionization is mainly induced by the multiphoton ionization; when γ is smaller than 1, tunneling ionization becomes dominant.[52] In Fig. 3(c), the Keldysh parameter is shown as a function of the laser intensity (the gray background highlights the operation range of our laser intensity) is larger than 1, which implies that photoionization

in our case is mainly induced by multiphoton ionization. It becomes clear that the "seeds" for the electron avalanche are, indeed, fed by multiphoton ionized electrons. This explains the generation mechanism of the AMPL and the reason why more than two photons are able to be absorbed during the AMPL process, as seen in the change of fit slops in Figs. 2(a) and 2(b).

The optical breakdown threshold for Au NPs induced by a strong electromagnetic field can be evaluated by the two-temperature model (TTM), taking the source term into account.[53,54] The criterion adopted here is that the optical breakdown occurs when the lattice temperature reaches the melting point of Au NP at 1045 K.[53] The temperature-dependent electron capacity and electron–phonon coupling are imposed to improve the calculating accuracy (see the supplementary material).[55] The calculated electron (red) and lattice (blue) temperatures vs time are shown in Fig. 3(d). The horizontal dashed black line represents the melting point of Au NPs at 1045 K. As we can see, the electron and phonon reach the thermal equilibrium after a time scale of picoseconds. According to the TTM calculation, a laser intensity of around 71 GW cm^{-2} is required for the lattice temperature to reach the melting point. This value is in agreement with the experimental threshold observed in Fig. 2(a).

TTM is able to evaluate the thermal damage threshold for bulk metals in the focus of a strong laser beam. However, the local field enhancement of specific plasmonic structures is omitted in such a model. To explore the excitation angle-dependent AMPL effect, as shown in Fig. 2(b), we simulated the near-field distribution around a single Au120–Al180 contacted heterodimer using the finite-difference time-domain (FDTD) method. As shown in Figs. 4(a) and 4(b), the near-field distributions at the fundamental frequency are compared. With the excitation along the long dimer axis, the highest electric field is clearly visible close to the touching point of the heterodimer. The local field for an excitation polarized along the long dimer axis [$E_{longitudinal} = (E_x^2 + E_y^2 + E_z^2)^{1/2}$] is more than four times stronger than that for an excitation polarized along the short dimer axis ($E_{transverse}$) when only the maximum local fields are considered. Instead, when considering the areas marked by the dashed white circles in Figs. 4(a) and 4(b), the electric field enhancement with the longitudinal excitation is on average 1.2 times larger than it is for the transverse case. At an incident intensity of 63 GW cm^{-2}, the lattice temperature evaluated with the TTM after

thermalization is below the damage threshold (black dashed line indicating the melting temperature of 1045 K), as shown in Fig. 4(c). When taking the averaged field enhancement factor of 1.2 into account, e.g., by tuning the excitation polarization from along the dimer short axis to the dimer long axis, the lattice temperature (blue dashed line) after thermalization is beyond the threshold, as seen in Fig. 4(c). This result indicates that the local field enhancement plays an important role in the excitation process, especially in the multiphoton absorption.[19,27] With longitudinal polarization excitation, the electric fields in the hot-spots are parallel to the dimer connections and the electric field can penetrate the dimers, resulting in strong multiphoton absorption.[19,27,4] On the other hand, when the incident wave is polarized perpendicular to the dimer long axis, the local electric field is mainly orthogonal to the NP surface and the internal field is somewhat reduced by the electron screening, limiting the absorption process.[19,27,4] Thus, the longitudinal excitation is beneficial for generating strong far-field MPL.

We now turn our attention to the emission process of AMPL. Interestingly, as shown in Fig. 5(a), the spectrally resolved power law exponent coefficients in post-AMPL cases show linear dependency on the emitted photon energy, rather than keeping a nearly constant value of 2 as is the case for the pre-AMPL step. The power law exponent coefficients, namely, the slope values in the double logarithmic plots of the emitted intensity vs photon energy, are marked with blue marks for the pre-AMPL case and red for the post-AMPL step. The contacted heterodimers used here are Au120–Al160 (square), Au200–Al120 (asterisks), Au120–Al220 (circle), Au120–Al140 (cross), and Au120–Al120 (diamond). The excitation beam is linearly polarized along the dimer long axis. The linear dependence of the power law exponent as a function of the emitted photon energy was observed by Haug et al.[56] and explained by the recombination of hot carriers. A theoretical model that combines thermodynamic properties of the nanoscale electron system with photonic mode density closely related to the specific plasmonic environment was proposed; it provides an approach to evaluate the emission intensity of AMPL (see the supplementary material).

We also find that a dramatic and irreversible spectral linewidth broadening occurs during the emission process of AMPL. At the pre-AMPL step, the emission spectra originate from the thermal radiation of hot electrons in the conduction bands, which are modulated by specific nanoantennas plasmon modes or the recombination
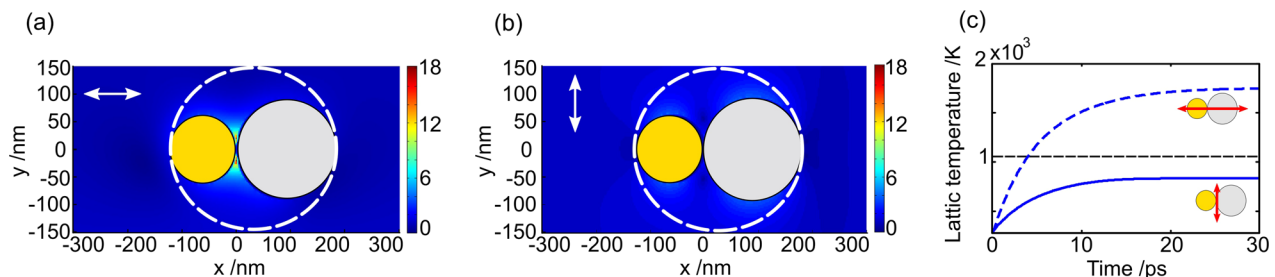
FIG. 4. [(a) and (b)] Fundamental near-field distributions around a single Au120–Al180 contacted heterodimer. The double-end white arrows indicate the polarization directions, which are either along the dimer long (a) or short (b) axis. The white dashed circles mark the areas in which the average field enhancement is evaluated. The scale bars denote the calculated local electric field enhancement factors. (c) Calculated lattice temperature vs time according to the two-temperature model at the laser intensity of 63 GW cm^{-2} under the transverse (solid curve) and longitudinal (dashed curve) excitation. The black horizontal dashed line represents the melting point of Au NPs: 1045 K.
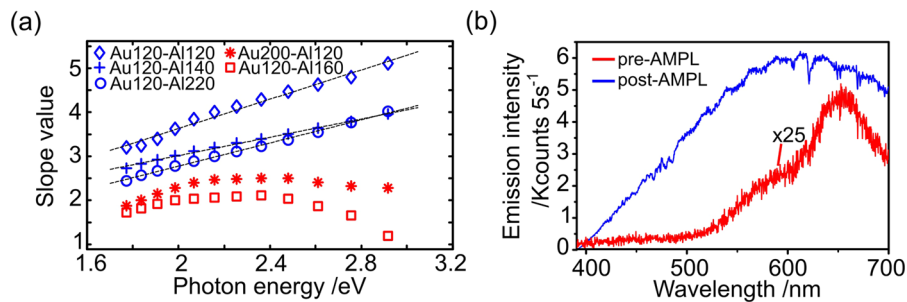
FIG. 5. (a) Power law exponent coefficients as functions of emitted photon energies in both pre-AMPL (red) and post-AMPL (blue) steps. The exponent coefficient in the post-AMPL stage is fitted by linear functions (black dashed lines). The contacted heterodimers are Au120–Al160 (square), Au200–Al120 (asterisks), Au120–Al220 (circle), Au120–Al140 (cross), and Au120–Al120 (diamond). The excitation beam is linearly polarized along the dimer long axis. (b) MPL spectra from a 50-nm thick Au film (black) and a single contacted Au120–Al160-g20 nanodimer before (red) and after (blue) the AMPL occurrence. The integrating time is 50 s and 5 s for the Au film and Au–Al NPs, respectively. For guiding the eyes, the emission signals of Au film and pre-AMPL are multiplied by 25. The incident beam is linearly polarized along the dimer long axis. AMPL occurs when the excitation polarization changes.

of excited carriers at specific high symmetric points of the first Brillouin zone, e.g., X or L symmetry points, due to the high optical density (OD).[20,27,37] The linewidth for such MPL spectra is small, as shown by the red curve in Fig. 5(b). However, during the post-AMPL step, the AMPL spectrum always exhibits a broad peak, starting from 400 nm and extending to our detectable limit (700 nm), as shown by the blue curve in Fig. 5(b). For guiding the eyes, the emission signals in pre-AMPL step are multiplied by a factor of 25. The incident beam is linearly polarized along the dimer long axis. As seen from Fig. 5(b), the MPL spectra after the occurrence of AMPL have a more blackbody-radiation-like profile. The broad linewidth could be caused by[57] (1) thermal radiations from the hot electrons in the conduction bands and lower energy bands; (2) interband transitions of excited carriers at other symmetric points from the same or different valence bands; (3) collisional broadening at high temperature. Further investigations are required to narrow these different hypotheses down.

IV. CONCLUSION

AMPL is observed from coupled Au–Al heterodimers when the incident beam exceeds a critical laser intensity or when the incident polarization is close to the longitudinal excitation. The emission intensity increases by more than one order of magnitude and encounters dramatic spectral changes. The corresponding intrinsic mechanisms are unveiled by a series of laser intensity- and polarization-dependent measurements on Au–Al heterodimers with varying diameters and gaps. The underlying physical mechanisms are explained via Keldysh's rate equation in strong-field. It is interpreted that AMPL derives from the recombination of avalanche ionized hot carriers seeded by multiphoton ionization. The multiphoton ionization can be assisted by the dramatic local field of coupled Au–Al nanoantennas at the excitation stage. The optical breakdown threshold can be predicted via a TTM model, taking the source term into account. The photon emission for AMPL can be evaluated as a function of the local field environment of a specific plasmonic nanostructure and the thermal factor of hot carriers, in accordance with the experimental linear relationship between power

law exponent coefficient and emitted photon energy. The change in the emission spectral profile of the electron–hole recombination is explained by the spectral linewidth broadening mechanisms. Our results provide systematic interpretations for the high spectral "background" in surface enhanced Raman spectroscopy or extraordinary fluorescence enhancement when high laser excitation power is used. The surface enhanced spectroscopy and currently emerging laser-induced breakdown spectroscopy could benefit from this investigation.

V. EXPERIMENTAL SECTION

A. Nanoantenna fabrication

Arrays of Au–Al heterodimers are fabricated on glass using double electron-beam lithography. The Au NP diameter changes from 80 nm to 200 nm with a step of 20 nm. For each Au NP size, the diameter of Al NP is varied from 120 nm to 240 nm with a step of 20 nm. The gap for each Au–Al heterodimer varies from the contact (no gap) to 200 nm with a step of 20 nm. The thickness of the NPs is 50 nm. The distance between each adjacent heterodimer is 10 μm, such that the nonlinear optical measurements can be performed at a single particle level with confocal microscopy. In order to have reference samples, the same sizes of homodimers and their corresponding monomers of the same dimensions are also fabricated. A detailed description of the fabrication procedure can be found in the "supplementary material."

B. Nonlinear optical characterization

The plasmonic nanostructures are characterized in a home-built sample-scanning confocal optical microscope. The optical path and its full description are shown in the supplementary material. Instead of using an objective lens, a parabolic mirror is employed to focus and to collect the optical signal. Thanks to the large numerical aperture (NA = 0.998) and chromatic aberration free focusing, the parabolic mirror allows us to achieve a tight focus of about 380 nm.[58,59] For optical excitation, a femtosecond laser generates ultra-short pulses (~110 fs, 89 MHz, 774 nm) in a TEM$_{00}$ Gaussian

mode. To modulate the incident power, a gradient gray filter is used. Once the optical density (OD) of the gradient gray filter is changed, the averaged laser power is measured in front of the parabolic mirror. The incident laser intensity is taken as e^{-2} of the peak intensity. All the incidence intensity values used in the manuscript are calculated considering the average laser power and the size of the laser focus in the parabolic mirror. To achieve the required polarization, the excitation beam is delivered through a lambda-half wave plate. The spectra are taken at the touching points for the contacted nanodimers and the gap centers for the gapped nanodimers, respectively. For the ones with sizes smaller than the dimension of the laser focus, the spectra are collected at the centers of Airy disks.

SUPPLEMENTARY MATERIAL

See the supplementary material for information about sample fabrication, experimental setup, and theoretical calculation.

ACKNOWLEDGMENTS

DATA AVAILABILITY

The data that support the findings of this study are available within the article and its supplementary material.

REFERENCES

[1] P. Bharadwaj, B. Deutsch, and L. Novotny, Adv. Opt. Photonics **1**, 438 (2009).

[2] M. Kauranen and A. V. Zayats, Nat. Photonics **6**, 737 (2012).

[3] S. A. Maier, *Plasmonics: Fundamentals and Applications* (Springer Science & Business Media, 2007).

[4] J. Wang, J. Butet, A.-L. Baudrion, A. Horrer, G. Lévêque, O. J. F. Martin, A. J. Meixner, M. Fleischer, P.-M. Adam, A. Horneber, and D. Zhang, J. Phys. Chem. C **120**, 17699 (2016).

[5] M. I. Stockman, Science **348**, 287 (2015).

[6] P. D. Howes, R. Chandrawati, and M. M. Stevens, Science **346**, 1247390 (2014).

[7] T. K. Ahn, T. J. Avenson, M. Ballottari, Y.-C. Cheng, K. K. Niyogi, R. Bassi, and G. R. Fleming, Science **320**, 794 (2008).

[8] J. Lin, H. Li, H. Zhang, and W. Chen, Appl. Phys. Lett. **102**, 203109 (2013).

[9] N. Guo, W.-D. Hu, X.-S. Chen, L. Wang, and W. Lu, Opt. Express **21**, 1606 (2013).

[10] L. Novotny and N. Van Hulst, Nat. Photonics **5**, 83 (2011).

[11] W. L. Barnes, A. Dereux, and T. W. Ebbesen, Nature **424**, 824 (2003).

[12] N. J. Halas, S. Lal, W.-S. Chang, S. Link, and P. Nordlander, Chem. Rev. **111**, 3913 (2011).

[13] M. Danckwerts and L. Novotny, Phys. Rev. Lett. **98**, 026104 (2007).

[14] J. Butet, P.-F. Brevet, and O. J. F. Martin, ACS Nano **9**, 10545 (2015).

[15] A. Horneber, A.-L. Baudrion, P.-M. Adam, A. J. Meixner, and D. Zhang, Phys. Chem. Chem. Phys. **15**, 8031 (2013).

[16] K. J. Russell, T.-L. Liu, S. Cui, and E. L. Hu, Nat. Photonics **6**, 459 (2012).

[17] J. Grand, P.-M. Adam, A.-S. Grimault, A. Vial, M. Lamy de la Chapelle, J.-L. Bijeon, S. Kostcheev, and P. Royer, Plasmonics **1**, 135 (2006).

[18] A. Konrad, F. Wackenhut, M. Hussels, A. J. Meixner, and M. Brecht, J. Phys. Chem. C **117**, 21476 (2013).

[19] J. Wang, J. Butet, G. D. Bernasconi, A.-L. Baudrion, G. Lévêque, A. Horrer, A. Horneber, O. J. F. Martin, A. J. Meixner, M. Fleischer, P.-M. Adam, and D. Zhang, Nanoscale **11**, 23475 (2019).

[20] G. T. Boyd, Z. H. Yu, and Y. R. Shen, Phys. Rev. B **33**, 7923 (1986).

[21] A. Mooradian, "Photoluminescence of metals," Phys. Rev. Lett. **22**, 185 (1969).

[22] R. Rosei, Phys. Rev. B **10**, 474 (1974).

[23] P. Winsemius, M. Guerrisi, and R. Rosei, Phys. Rev. B **12**, 4570 (1975).

[24] H. Hu, H. Duan, J. K. W. Yang, and Z. X. Shen, ACS Nano **6**, 10147 (2012).

[25] A. Bouhelier, R. Bachelot, G. Lerondel, S. Kostcheev, P. Royer, and G. Wiederrecht, Phys. Rev. Lett. **95**, 267405 (2005).

[26] A. Horneber, K. Braun, J. Rogalski, P. Leiderer, A. J. Meixner, and D. Zhang, Phys. Chem. Chem. Phys. **17**, 21288 (2015).

[27] J. Wang, E. Gürdal, A. Horneber, S. Dickreuter, S. Kostcheev, A. J. Meixner, M. Fleischer, P.-M. Adam, and D. Zhang, Nanoscale **10**, 8240 (2018).

[28] J. Wang, A. Coillet, O. Demichel, Z. Wang, D. Rego, A. Bouhelier, P. Grelu, and B. Cluzel, Light: Sci. Appl. **9**, 50 (2020).

[29] K. Schraml, A. Regler, J. Bartl, G. Glashagen, J. Wierzbowski, J. J. Finley, and M. Kaniber, Optica **3**, 1453 (2016).

[30] O. Demichel, M. Petit, S. Viarbitskaya, R. Méjard, F. De Fornel, E. Hertz, F. Billard, A. Bouhelier, and B. Cluzel, ACS Photonics **3**, 791 (2016).

[31] R. Méjard, A. Verdy, M. Petit, A. Bouhelier, B. Cluzel, and O. Demichel, ACS Photonics **3**, 1482 (2016).

[32] P. Biagioni, M. Celebrano, M. Savoini, G. Grancini, D. Brida, S. Mátéfi-Tempfli, M. Mátéfi-Tempfli, L. Duò, B. Hecht, and G. Cerullo, Phys. Rev. B **80**, 045411 (2009).

[33] Z. Ma, Y. Yu, S. Shen, H. Dai, L. Yao, Y. Han, X. Wang, J.-B. Han, and L. Li, Sci. Rep. **6**, 18857 (2016).

[34] Q.-Q. Wang, J.-B. Han, D.-L. Guo, S. Xiao, Y.-B. Han, H.-M. Gong, and X.-W. Zou, Nano Lett. **7**, 723 (2007).

[35] H. M. Gong, Z. K. Zhou, S. Xiao, X. R. Su, and Q. Q. Wang, Plasmonics **3**, 59 (2008).

[36] M. Song, G. Chen, Y. Liu, E. Wu, and H. Zeng, Opt. Express **20**, 22290 (2012).

[37] K. Imura, T. Nagahara, and H. Okamoto, J. Phys. Chem. B **109**, 13214 (2005).

[38] X.-F. Jiang, Y. Pan, C. Jiang, T. Zhao, P. Yuan, T. Venkatesan, and Q.-H. Xu, J. Phys. Chem. Lett. **4**, 1634 (2013).

[39] M. Castro-Lopez, D. Brinks, R. Sapienza, and N. F. van Hulst, Nano Lett. **11**, 4674 (2011).

[40] E. D. Palik, *Handbook of Optical Constants of Solids* (Akademic Press, Orlando, FL, 1985), p. 1.

[41] C.-K. Sun, F. Vallée, L. H. Acioli, E. P. Ippen, and J. G. Fujimoto, Phys. Rev. B **50**, 15337 (1994).

[42] S. Link, C. Burda, Z. L. Wang, and M. A. El-Sayed, J. Chem. Phys. **111**, 1255 (1999).

[43] J. Hohlfeld, S.-S. Wellershoff, J. Güdde, U. Conrad, V. Jähnke, and E. Matthias, Chem. Phys. **251**, 237–258 (2000).

[44] J. Noack and A. Vogel, IEEE J. Quantum Electron. **35**, 1156 (1999).

[45] A. P. Joglekar, H.-h. Liu, E. Meyhöfer, G. Mourou, and A. J. Hunt, Proc. Natl. Acad. Sci. U. S. A. **101**, 5856 (2004).

[46] B. C. Stuart, M. D. Feit, S. Herman, A. M. Rubenchik, B. W. Shore, and M. D. Perry, J. Opt. Soc. Am. B **13**, 459 (1996).

[47] S. Musazzi and U. Perini, *Laser-Induced Breakdown Spectroscopy* (Springer, 2014), p. 182.

[48] I. Sow, J. Grand, G. Lévi, J. Aubard, N. Félidj, J.-C. Tinguely, A. Hohenau, and J. R. Krenn, J. Phys. Chem. C **117**, 25650 (2013).

[49] S. Amoruso, X. Wang, C. Altucci, C. De Lisio, M. Armenante, R. Bruzzese, N. Spinelli, and R. Velotta, Appl. Surf. Sci. **186**, 358 (2002).

[50] Z. Zhang, P. A. VanRompay, J. A. Nees, and P. P. Pronko, J. Appl. Phys. **92**, 2867 (2002).

[51] S. Amoruso, X. Wang, C. Altucci, C. De Lisio, M. Armenante, R. Bruzzese, and R. Velotta, Appl. Phys. Lett. **77**, 3728 (2000).

[52] L. V. Keldysh, Sov. Phys. JETP **20**, 1307 (1965).

[53] N. Wang, S. I. Rokhlin, and D. F. Farson, J. Nanopart. Res. **13**, 4491 (2011).

[54] S.-S. Wellershoff, J. Hohlfeld, J. Güdde, and E. Matthias, Appl. Phys. A **69**, S99 (1999).

[55] Z. Lin, L. V. Zhigilei, and V. Celli, Phys. Rev. B **77**, 075133 (2008).

[56] T. Haug, P. Klemm, S. Bange, and J. M. Lupton, Phys. Rev. Lett. **115**, 067403 (2015).

[57] W. Demtröder, *Laser Spectroscopy* (Springer, 2008), p. 1.

[58] P. Reichenbach, A. Horneber, D. A. Gollmer, A. Hille, J. Mihaljevic, C. Schäfer, D. P. Kern, A. J. Meixner, D. Zhang, and M. Fleischer, Opt. Express **22**, 15484 (2014).

[59] M. A. Lieb and A. J. Meixner, Opt. Express **8**, 458 (2001).